High-performance near-field thermophotovoltaics based on a $CaCO_3$/graphene/InSb heterostructure

Lin Li,[1] Kun Yu,[1] Dudong Feng,[2] Zhimin Yang,[3] Kaihua Zhang,[1] Yufang Liu,[1] and Xiaohu Wu[4,*]

[1] *Henan Key Laboratory of Infrared Materials & Spectrum Measures and Applications, School of Physics, Henan Normal University, Xinxiang 453007, People's Republic of China*

[2] *School of Mechanical Engineering and the Birck Nanotechnology Center, Purdue University, West Lafayette, IND 47907, USA*

[3] *School of Physics and Electronic Information, Yan'an University, Yan'an 716000, People's Republic of China*

[4] *Shandong Institute of Advanced Technology, Jinan 250100, People's Republic of China*

(Received 29 March 2023; revised 7 October 2023; accepted 7 November 2023; published 8 December 2023)

Due to the contribution of photon tunneling, the output power of near-field thermophotovoltaic (NFTPV) devices can surpass that of far-field thermophotovoltaic devices by several orders of magnitude, which has recently drawn extensive attention. Previous research explores the enhancement brought by hyperbolic materials, but little investigation has been done on the frequency shift of hyperbolic bands. Hyperbolic metamaterials acquire the hyperbolic properties through complex nanofabrication processes. However, calcite ($CaCO_3$), as a natural hyperbolic material, possesses hyperbolic properties without the need for expensive processing. Despite this, $CaCO_3$ is rarely chosen as the thermal emitter in NFTPV devices. In this work, we propose an NFTPV device using $CaCO_3$ as the thermal emitter and an InSb *p-n* junction as the PV cell. Furthermore, we compare the performance of four structures to analyze the effect of the graphene layer on the $CaCO_3$-InSb NFTPV devices we propose. The numerical results demonstrate that the $CaCO_3$/graphene/InSb structure exhibits the best performance based on the assumption of considering only radiative recombination. The $CaCO_3$/graphene/InSb structure simultaneously achieves 41% efficiency and 94 W/cm^2 output power density when the temperature of the thermal emitter is 900 K. The physical mechanism of the significantly improved performance of the NFTPV device arises from the frequency coupling between the hyperbolic resonance and the interband transition of the InSb *p-n* junction, where the surface plasmon polaritons excited in graphene make a promotion role. Moreover, we discuss the impact of the gap distance, the temperature of the thermal emitter, and the thickness of the thermal emitter on the performance of NFTPV devices. Our research contributes to understanding the coupling of surface plasmon polaritons and hyperbolic phonon polaritons and the design of high-performance thermophotovoltaic device.

DOI: 10.1103/PhysRevApplied.20.064015

I. INTRODUCTION

Thermophotovoltaic (TPV) cells have garnered significant attention as solid-state heat engines that can efficiently convert infrared light into electric energy. Compared to turbine-based generators, TPV cells offer superior performance in extracting work from any heat source [1–10]. As a result, TPV cells hold promising prospects in various applications, including thermal energy-storage systems [11,12], solar radiation [13–16], combustion [17,18], and waste heat recovery [19]. Their ability to effectively harness and convert thermal energy makes TPV cells a viable solution in these fields.

A TPV system is comprised of a thermal emitter and a photovoltaic (PV) cell. Typically, the thermal emitter is made of either metal or hyperbolic metamaterials, while the PV cell consists of semiconductor *p-n* junctions. Remarkable amplification of near-field radiative heat transfer (NFRHT) can occur when the distance between the thermal emitter and PV cell is smaller than the characteristic thermal wavelength. This amplification is a result of the contribution of coupled evanescent waves. The excitation of surface plasmon polaritons (SPPs) [20–24] and surface phonon polaritons (SPhPs) [25–27] further enhances the performance of the near-field thermophotovoltaic (NFTPV) device. In addition, hyperbolic materials (HMs) are used as thermal emitters. Hyperbolic phonon polaritons (HPhPs) [28–34] with a narrow-band characteristic assist in achieving a high-performance NFTPV device [35,36].

*xiaohu.wu@iat.cn

 © 2023 American Physical Society

$CaCO_3$, a natural HM, holds great potential in enhancing the performance of NFTPV devices due to its hyperbolic dispersion in wavevector space, which can support high wavevector modes. In TPV systems, InSb is commonly employed as a narrow band gap semiconductor [7,8,35,36]. However, there is still a considerable mismatch between the frequency of the band gap of InSb and the emission spectrum of $CaCO_3$. A recent study by Zhang *et al.* investigated the impact of the optical axis (OA) orientation of $CaCO_3$ on the NFRHT between two parallel $CaCO_3$ structures. It was found that by changing the orientations of the OA, the spectrum of $CaCO_3$ can be reshaped, potentially allowing for the absorption of more useful photons and thereby boosting the performance of the NFTPV device [37]. Additionally, Messina *et al.* proposed a graphene-covered TPV device and demonstrated that it can improve the efficiency of the TPV cell and the produced current, highlighting the potential of graphene in enhancing the performance of NFTPV devices [8]. Despite these potential benefits, there is currently a lack of research on the use of $CaCO_3$ as a thermal emitter in NFTPV devices. Therefore, further investigation is necessary to fully explore the potential of $CaCO_3$ and determine its effectiveness in this application.

In this work, we present an NFTPV device utilizing $CaCO_3$ as the thermal emitter and an InSb p-n junction as the PV cells. To analyze the effects of a graphene layer on the performance of the $CaCO_3$-InSb NFTPV devices, we compare four different structures: (i) $CaCO_3$-InSb, the initial structure; (ii) $CaCO_3$-G/InSb, where the InSb p-n junction is covered with a graphene layer; (iii) $CaCO_3$/G-InSb, where the thermal emitter is covered with a graphene layer; and (iiii) $CaCO_3$/G-G/InSb, where both the thermal emitter and PV cell are covered with a graphene layer. Additionally, we investigate the impact of the gap distance, temperature of the thermal emitter, and thickness of the thermal emitter on the performance of the NFTPV devices.

II. MODELING AND METHODS

The schematic diagram of the NFTPV device is shown in Fig. 1. Four designs are set up in this work, namely (i) $CaCO_3$-InSb, (ii) $CaCO_3$-G/InSb, (iii) $CaCO_3$/G-InSb, and (iiii) $CaCO_3$/G-G/InSb. The gap distance is d, the chemical potential μ_g of graphene is 1.0 eV, the thickness of the thermal emitter is h, and the PV cell is semi-infinite. The temperatures of the thermal emitter and PV cell are T_{emit} and T_{cell}, respectively. Notably, the temperature of the graphene layer is the same as the attached surface.

$CaCO_3$ is a uniaxial HM with two Reststrahlen bands (RBs). When the OA of $CaCO_3$ is aligned with the x axis, the permittivity is expressed by the following equation [37]:

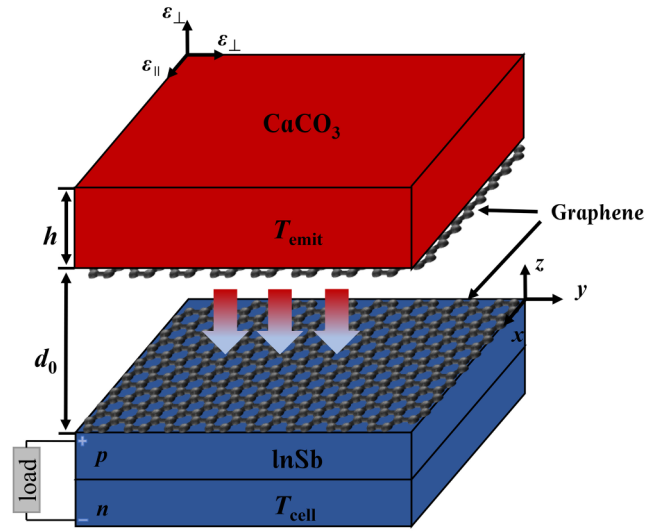

FIG. 1. Schematic illustration of NFTPV devices. The NFRHT between the emitter and absorber is aligned with the z axis.

$$\varepsilon = \begin{bmatrix} \varepsilon_\parallel & 0 & 0 \\ 0 & \varepsilon_\perp & 0 \\ 0 & 0 & \varepsilon_\perp \end{bmatrix}$$

$$\varepsilon_m = \varepsilon_{\infty,m}\Pi_j\left(1 + \frac{\omega_{\text{LO},m}^2 - \omega_{\text{TO},m}^2}{\omega_{\text{TO},m}^2 - \omega^2 + j\Gamma_m\omega}\right), m = \perp, \parallel, \tag{1}$$

where $m = \perp$, $\parallel$ for the permittivity either parallel or perpendicular to the z axis, ω is the angular frequency. Relevant parameters are obtained from Ref. [37].

The real permittivity components of $CaCO_3$ are shown in Fig. 2. The spectral ranges of type-I hyperbolic band (band 2) and type-II hyperbolic band (band 3) are in the regions of 1.63–1.75×10^{14} rad/s and 2.64–3.18×10^{14} rad/s, respectively [37].

The optical properties of the graphene layer are expressed by the electrical conductivity σ_g, which consists of intraband σ_D and interband σ_I, i.e., $\sigma_g = \sigma_D + \sigma_I$. The equation can be calculated by the following equations [38,39]:

$$\sigma_D = \frac{i}{\omega + i/\tau}\frac{2e^2 k_B T_g}{\pi\hbar^2}\ln\left[2\cosh\left(\frac{\mu_g}{2k_B T_g}\right)\right], \tag{2}$$

$$\sigma_I = \frac{e^2}{4\hbar}\left[G\left(\frac{\hbar\omega}{2}\right) + i\frac{4\hbar\omega}{\pi}\int_0^\infty \frac{G(\xi) - G(\hbar\omega/2)}{(\hbar\omega)^2 - 4\xi^2}d\xi\right], \tag{3}$$

$$G(\xi) = \sinh\left(\frac{\xi}{K_B T_g}\right)\Big/\left[\cosh\left(\frac{\xi}{K_B T_g}\right) + \cosh\left(\frac{\mu_g}{K_B T_g}\right)\right], \tag{4}$$

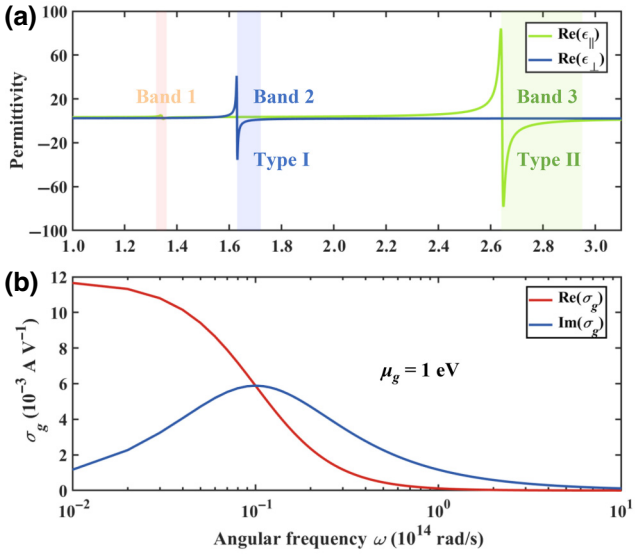

FIG. 2. (a) The real permittivity components of $CaCO_3$. (b) The real and imaginary parts of graphene conductivity vary with frequency.

where $G(\xi)$ denotes a dimensionless function. τ denotes the electron scattering time set to 100 fs [40]. T_g denotes the temperature of the graphene layer. e, K_B, $\hbar$ denote the electron charge, Boltzmann constant, and reduced Planck constant, respectively.

We aim to increase the spectral heat transfer above the band gap of InSb and reduce that under the band gap of InSb. The reason is that the photovoltaic effect generates electron-hole pairs (EHPs) only when photons with energy above the band gap emitted by the thermal emitter are absorbed by the PV cell. In addition, photons below the band gap frequency do not possess enough energy to generate EHPs but cause parasitic heating and thus reduce the efficiency of the NFTPV device.

The permittivity of InSb is expressed by the following equation [41]:

$$\varepsilon = \left(n + \frac{ic\alpha(\omega)}{2\omega}\right)^2, \tag{5}$$

where the refractive index $n = 3.96$ [42] and c is the speed of light in vacuum. $\alpha(\omega)$ is a step function describing the photon absorption, as follows:

$$\alpha(\omega) = \begin{cases} 0, & \omega \le \omega_{\text{gap}} \\ \alpha_0\sqrt{\omega/\omega_{\text{gap}} - 1}, & \omega \ge \omega_{\text{gap}} \end{cases}, \tag{6}$$

where the absorption rate $\alpha_0 = 0.7\ \mu\text{m}^{-1}$. ω_{gap} denotes the angular frequency corresponding to the band gap of InSb, which is calculated by the following equation:

$$\omega_{\text{gap}} = \frac{\text{e}E_{\text{gap}}}{\hbar}. \tag{7}$$

E_{gap} is the temperature-dependent band gap energy of InSb [43]:

$$E_{\text{gap}} = 0.24 - 6 \times 10^{-4}\frac{{T_{\text{cell}}}^2}{{T_{\text{cell}}}^2 + 500}, \tag{8}$$

where the band-gap energy $E_{\text{gap}} = 0.17$ eV and $\omega_{\text{gap}} = 2.62 \times 10^{14}$ rad/s when $T_{\text{cell}} = 300$ K.

The NFRHT between the emitter and absorber is calculated by the following equation [1]:

$$\begin{aligned} Q_{\text{above}} &= \int_{\omega_{\text{gap}}}^{+\infty} [\Theta(\omega, T_{\text{emit}}, 0) - \Theta(\omega, T_{\text{cell}}, V)]\Phi(\omega)d\omega \\ Q_{\text{under}} &= \int_{0}^{\omega_{\text{gap}}} [\Theta(\omega, T_{\text{emit}}, 0) - \Theta(\omega, T_{\text{cell}}, 0)]\Phi(\omega)d\omega \end{aligned}, \tag{9}$$

where Q_{above} and Q_{under} are the net energy between the emitter and absorber at the upper and lower of the bandgap, respectively. $\Theta(\omega, T, V) = \hbar\omega/\{\exp[(\hbar\omega - eV)/K_BT] - 1\}$ represents the mean energy of Planck thermal harmonic oscillator. V denotes the voltage. At $\omega \le \omega_{\text{gap}}$, $V = 0$.

In Eq. (9), $\Phi(\omega)$ is the spectral heat flux (SHF) and is calculated by the following [44]:

$$\Phi(\omega) = \frac{1}{8\pi^3}\int_0^{2\pi}\int_0^{\infty} \xi(\omega, \beta, \phi)\beta d\beta d\phi, \tag{10}$$

where β represents the parallel wavevector; ϕ denotes the azimuthal angle. $\xi(\omega, \beta, \phi)$ represents the energy transmission coefficients (ETCs), which can be calculated by the following equation:

$$\xi(\omega, \beta, \phi) = \begin{cases} \text{Tr}[(\mathbf{I} - \mathbf{R_2^*R_2} - \mathbf{T_2^*T_2})\mathbf{D}(\mathbf{I} - \mathbf{R_1^*R_1} \\ \quad -\mathbf{T_1^*T_1})\mathbf{D}^*], \beta < k_0 \\ \text{Tr}[(\mathbf{R_2^*} - \mathbf{R_2})\mathbf{D}(\mathbf{R_1} - \mathbf{R_1^*})\mathbf{D}^*] \\ \quad e^{-2|k_z|d}, \beta > k_0 \end{cases}, \tag{11}$$

where $k_0 = \omega/c$ denotes the vacuum wave vector. 1 and 2 denote the thermal emitter and cell, respectively. Note that $k_z = \sqrt{k_0^2 - \beta^2}$ denotes the perpendicular wave-vector component in vacuum, and d denotes the gap between the two bodies. $\mathbf{R}$ and $\mathbf{T}$ denote p or s polarization Fresnel's reflection and transmission coefficients, which are calculated by the following equation:

$$\mathbf{R}_{1,2} = \begin{bmatrix} r_{ss}^{1,2} & r_{sp}^{1,2} \\ r_{ps}^{1,2} & r_{pp}^{1,2} \end{bmatrix}, \mathbf{T}_{1,2} = \begin{bmatrix} t_{ss}^{1,2} & t_{sp}^{1,2} \\ t_{ps}^{1,2} & t_{pp}^{1,2} \end{bmatrix}, \tag{12}$$

where $\mathbf{D}$ denotes a Fabry-Perot-like denominator matrix and can be calculated by $\mathbf{D} = (\mathbf{I} - \mathbf{R}_1\mathbf{R}_2e^{2jk_zd})^{-1}$. Relevant parameters are obtained from Ref. [45].

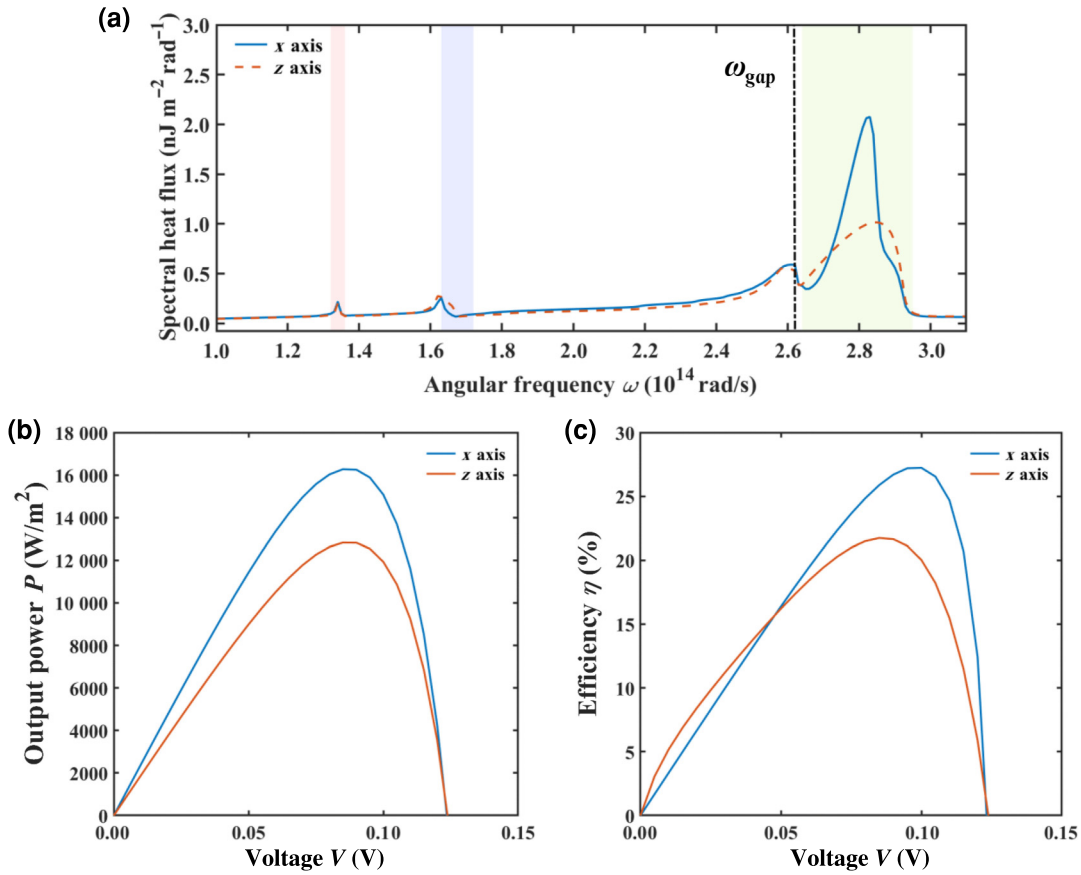

FIG. 3. (a) SHF of the $CaCO_3$-InSb structure with different OAs. (b) The output power P of the $CaCO_3$-InSb structure with different optical axes. (c) The efficiency η of the $CaCO_3$-InSb structure with different optical axes. Here, the thermal emitter is bulk, d is 20 nm, T_{emit} is 900 K, and T_{cell} is 300 K.

Based on the detailed balance analysis, we calculated the performance of different structures [42,46]. The current density J in the cell can be calculated by the following equation:

$$J = e\,[F_{12}(0) - F_{21}(V)], \tag{13}$$

where e is the elementary charge. In this work, we consider only radiative recombination and ignore nonradiative recombination (Auger recombination, etc.). F_{ij} represents the number flux of photons of energy above the band gap from object i to j, with subscript 1 representing the emitter and 2 representing the cell [1]:

$$F_{ij} = \int_{\omega_{gap}}^{+\infty} \frac{\Theta(\omega, T_i, V_i)}{\hbar\omega} \Phi(\omega) d\omega. \tag{14}$$

We assume that all incident photons are absorbed and that each photon with energy more remarkable than the band gap produces an EHP. The approximation is widely used in Refs. [8,47].

The output electric power density P can be calculated from

$$P = JV. \tag{15}$$

The efficiency η is calculated using

$$\eta = \frac{P}{Q_{under} + Q_{above}} \times 100\%. \tag{16}$$

III. RESULTS AND DISCUSSIONS

First, we analyze the performance of the NFTPV system consisting of $CaCO_3$ with different orientations of OA and InSb cell. When the OA is along the x axis, $CaCO_3$ has excellent in-plane anisotropy. Therefore, the excitation of volume-confined and surface-confined hyperbolic polaritons in $CaCO_3$ further promotes the NFRHT. As shown in Fig. 3(a), when the OA is along the x axis (case A), the SHF between the $CaCO_3$-InSb structure is greater than when the OA is along the z axis (case B) in band 3. In addition, the frequency range of band 3 is above the band gap frequency. Therefore, more useful photons can

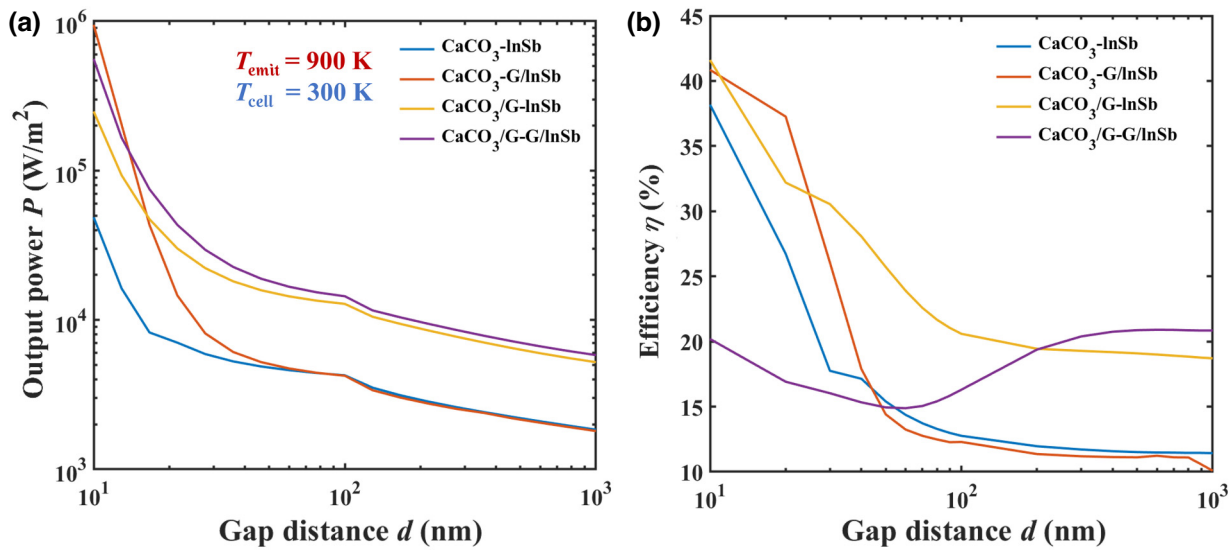

FIG. 4. The output power P and efficiency η vary with the gap distance for four structures. (a) Output power. (b) Efficiency. Here, the thermal emitter is bulk.

be absorbed, improving the performance of NFTPV systems. The output power P of case A is also larger than case B, as shown in Fig. 3(b). Furthermore, case A performs better in efficiency when voltage V gets a larger value, as shown in Fig. 3(c). Specifically, the output power P and maximum efficiency η of case A are 1.62 W/cm^2 and 27.2%, respectively, 0.34 W/cm^2 and 5.5% higher than that of case B. Thus, we mainly study the performance of NFTPV devices using $CaCO_3$ with OA along the x axis as the thermal emitter in this work.

Then, Fig. 4 show the output power and efficiency as a function of the gap distance d for the above four structures. Due to the reduction of NFRHT, the output power of four structures decreases monotonically with the increase of the gap distance d. Moreover, the four structures have different performances in different gap distances. As shown in Figs. 4(a) and 4(b), the $CaCO_3$-G/InSb structure has the highest output power when $d \leq 20$ nm. Specifically, the output power and efficiency of the $CaCO_3$-G/InSb structure are 94 W/cm^2 and 41% at $d = 10$ nm, respectively. We find that the output power of the $CaCO_3$-G/InSb structure decreases rapidly with the increase of d and has the lowest power (0.18 W/cm^2) at $d = 1000$ nm. In addition, the output power of the $CaCO_3$-InSb structure is almost the lowest at any distance. Figure 4(b) shows that the efficiency of the $CaCO_3$-G/InSb structure is almost the highest when $d < 20$ nm. With the increase of d, the $CaCO_3$/G-InSb structure gradually has the highest efficiency, and the efficiency of the $CaCO_3$-G/InSb structure decreases rapidly. However, the efficiency of the $CaCO_3$/G-G/InSb structure decreases first and then increases as d increases. At $d = 1000$ nm, the efficiency of the $CaCO_3$/G-G/InSb

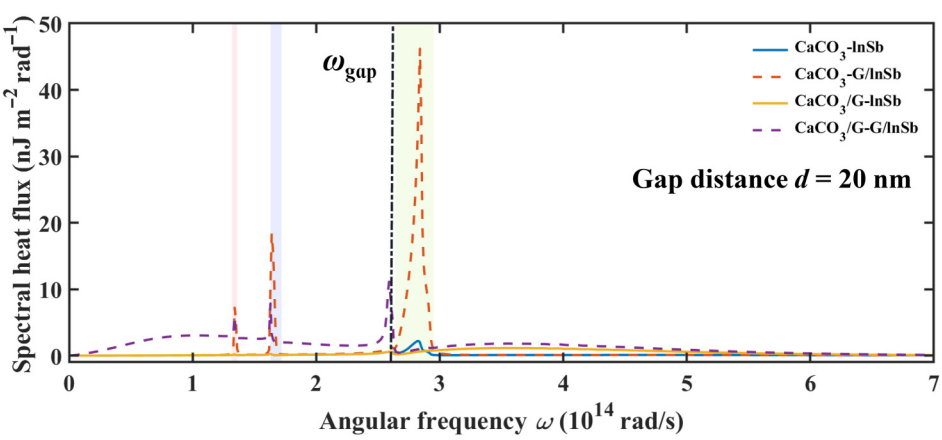

FIG. 5. SHFs vary with angular frequency for the four structures. The $\omega_{gap} = 2.62 \times 10^{14}$ rad/s, the T_{emit} is 900 K, and T_{cell} is 300 K, and the thermal emitter is bulk.

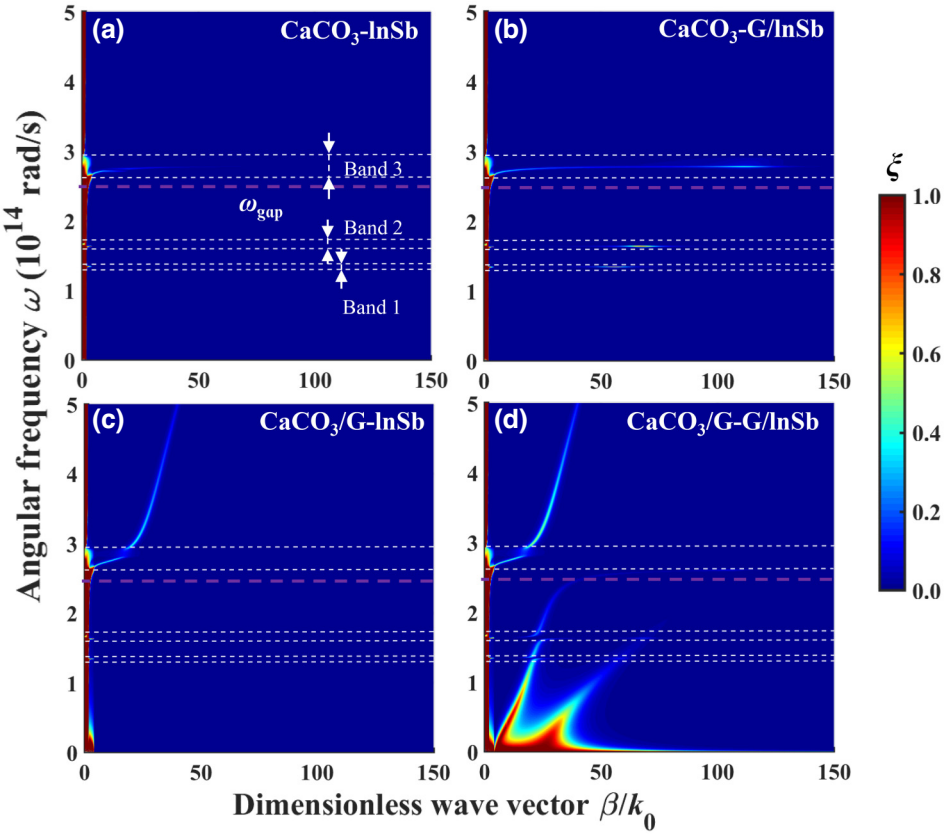

FIG. 6. ETCs between the thermal emitter and PV cell for different structures vary with angular frequency and dimensionless wavevector. (a) $CaCO_3$-InSb; (b) $CaCO_3$-G/InSb; (c) $CaCO_3$/G-InSb; (d) $CaCO_3$/G-G/InSb. The d is 20 nm, and the thermal emitter is bulk.

structure is the highest. Thus, the graphene layer significantly impacts the performance of the NFTPV device.

To analyze the mechanism responsible for different performances, we show the SHF of the four structures in Fig. 5. We find that the SHFs of the $CaCO_3$-InSb and $CaCO_3$-G/InSb structure are mainly enhanced in band 1, 2, and 3 of $CaCO_3$. In addition, the SHFs of $CaCO_3$/G-InSb and $CaCO_3$/G-G/InSb structures are enhanced in a wide range of frequencies. The physical mechanism of these SHF changes can be better illustrated by analyzing the ETCs, as shown in Fig. 6.

In the range above the band gap frequency, the SHF of the $CaCO_3$-G/InSb structure increases significantly compared with other structures since the resonant coupling of HPhPs and SPPs enhances the photon tunneling. The heat flux corresponding to the radiation recombination far exceeds the parasitic heat (lower than the band-gap energy) that cannot generate electricity. This is the key to designing solid-state heat engines with high conversion efficiency. Due to the resonant coupling of HPhPs and SPPs, the maximum power output of the $CaCO_3$-G/InSb structure is 19 times that of the $CaCO_3$-InSb structure. Moreover, because the SHF of $CaCO_3$/G-InSb and $CaCO_3$/G-G/InSb is enhanced in a wide range, the maximum output power of both is 5 and 11 times that of $CaCO_3$-InSb, respectively. The improvement of output power due to coupling polariton is predictable and will be discussed in the following context. However, the SHF of $CaCO_3$/G-G/InSb structures under the band gap frequency is also significantly boosted. Therefore, the parasitic loss is increased, resulting in the reduction of the efficiency of the $CaCO_3$/G-G/InSb structure.

The significant increase in the local density of states resulting from the support of high-β modes by hyperbolic materials leads to the enhancement in the emission of an emitter. The isotropic two-dimensional (2D) plasmonic material graphene can also greatly enhance emission of an emitter beyond its hyperbolic region by utilizing the support of surface plasmons [48,49]. To elucidate the coupling of HPhPs excited in $CaCO_3$ and SPPs excited in graphene for different NFTPV structures, we further calculate the ETCs as a function of angular frequency and dimensionless wavevector for different structures. In Fig. 6, bright regions represent high ETCs. As shown in Fig. 6(a), due to the hyperbolic characteristic of $CaCO_3$, the ETCs between $CaCO_3$-InSb structures are enhanced only in three bands. Specifically, ETCs in band 3 are enhanced significantly.

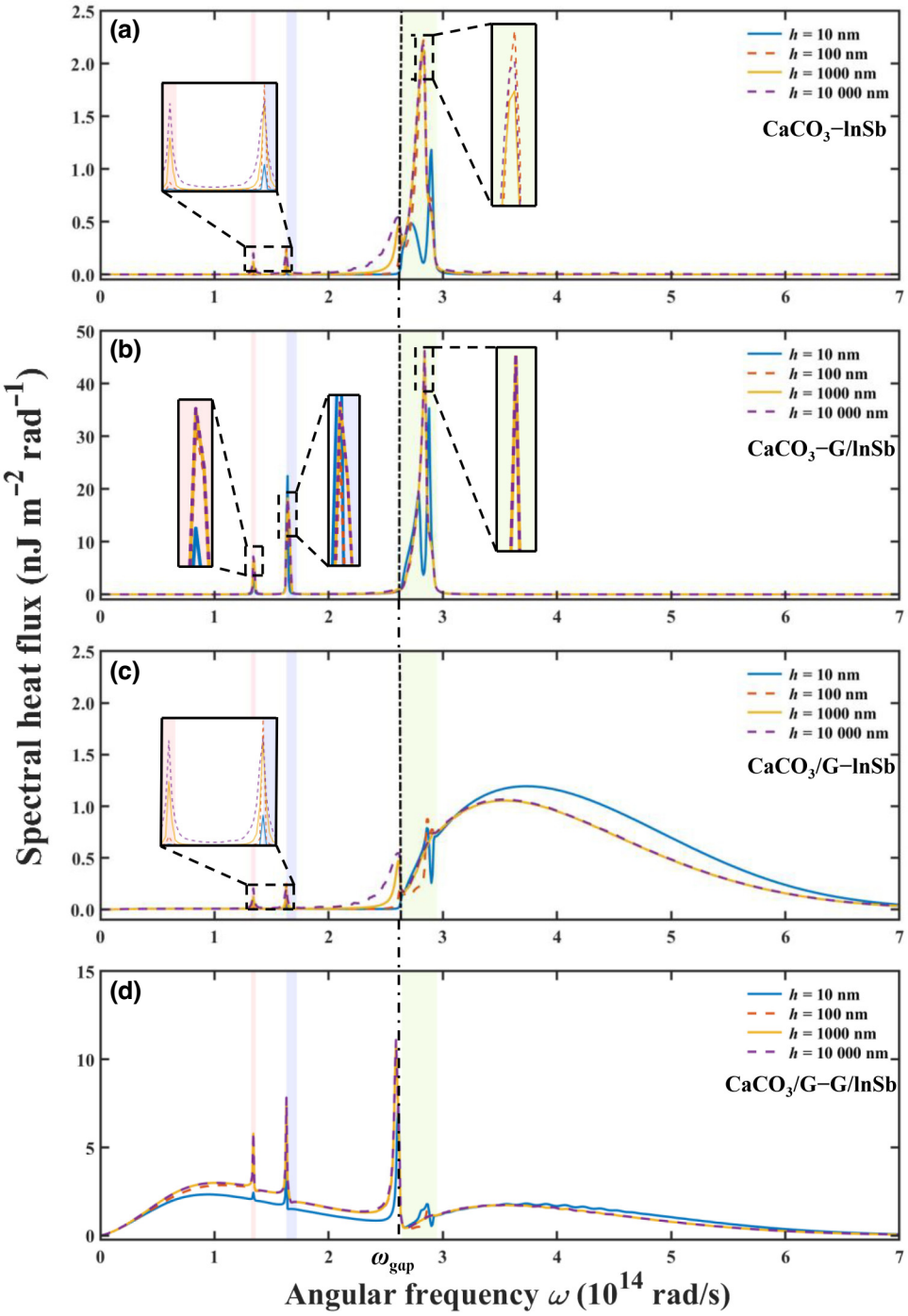

FIG. 7. SHFs of thermal emitters with different thicknesses vary with angular frequency for four structures. (a) $CaCO_3$-InSb. (b) $CaCO_3$-G/InSb. (c) $CaCO_3$/G-InSb. (d) $CaCO_3$/G-G/InSb. Here, d is 20 nm, T_{emit} is 900 K, and T_{cell} is 300 K.

When attaching the graphene to the p-n junction, ETCs between $CaCO_3$-G/InSb structures can be found to be further boosted in band 3 (above E_{gap}), which explains the strong photon emission in band 3 in Fig. 5. However, due to the enhanced ETC in bands 1 and 2, parasitic losses under the band gap frequency are increased, which is the main reason for the significant increase in output power while efficiency is limited, as shown in Fig. 6(b). These enhancements of ETCs are attributed to the frequency coupling between the hyperbolic resonance and the interband transition of InSb p-n junction.

When graphene is attached to the thermal emitter and p-n junction, ETCs between the $CaCO_3$/G-G/InSb structure can be enhanced in a larger region of wavevector

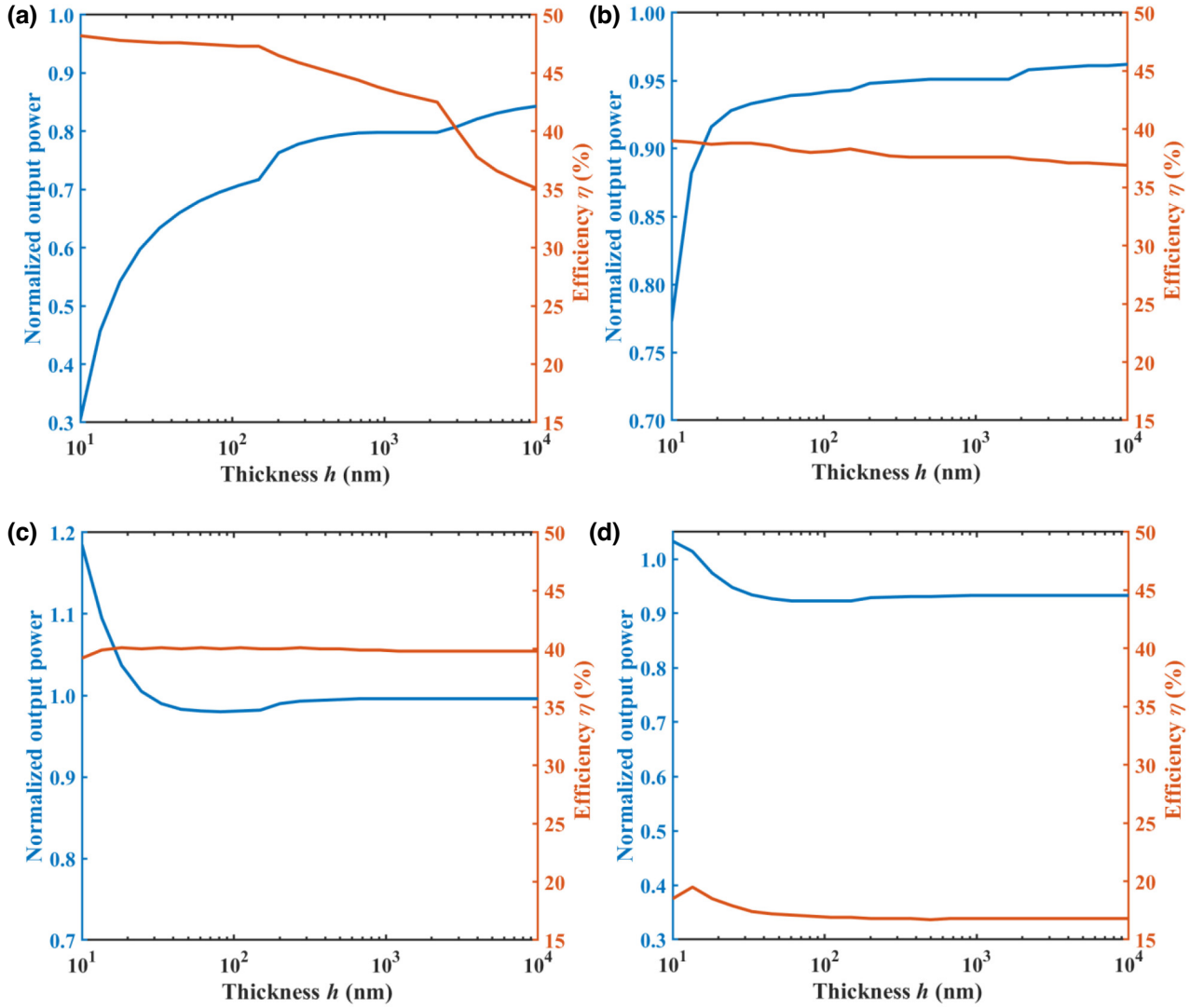

FIG. 8. The output power and efficiency of four structures vary with different thicknesses. (a) $CaCO_3$-InSb. (b) $CaCO_3$-G/InSb. (c) $CaCO_3$/G-InSb. (d) $CaCO_3$/G-G/InSb. The normalized output power refers to the ratio of the output power at a certain thermal emitter thickness to the output power when the thermal emitter is semi-infinite. Here, d is 20 nm, T_{emit} is 900 K, and T_{cell} is 300 K.

space, as shown in Fig. 6(d). In the range above the band-gap frequency, we find that the coupling between SPPs in graphene and HPhPs in $CaCO_3$ forms a kind of hybrid polariton, the surface plasmon phonon polaritons (SPPPs). The enhanced ETCs in a wide frequency range are mainly caused by the frequency coupling between the interband transition of InSb and the SPPPs. This results in a wide range of photon emissions, improving the output power of the $CaCO_3$/G-G/InSb structure. In addition, the enhancements of ETCs under the band gap frequency are mainly contributed by the coupling of SPPs in graphene. The two branches are attributed to the evanescent coupling between two closely spaced graphene layers that split the SPPs dispersion. Nevertheless, these can lead to significant parasitic loss, which decreases the efficiency of NFTPV devices.

Similarly, the ETCs between $CaCO_3$/G-InSb structures mainly enhanced in the wavevector space above the band gap frequency, which is contributed by the frequency coupling between the interband transition of InSb and the SPPPs, as shown in Fig. 6(c). Since no graphene is attached to the p-n junction, ETCs under band gap frequency are not significantly enhanced. From the above analysis, the physical mechanisms of the graphene layer affecting the performance of NFTPV devices are clearly understood.

Previous studies show that the thickness of HMs significantly affects the NFRHT [50–54]. Therefore, we study the impact of $CaCO_3$ thickness on the performance of NFTPV devices. We find that when the thickness $h = 10$ nm, the SHF of $CaCO_3$-InSb and $CaCO_3$-G/InSb structures is very low compared with other thicknesses, limiting the output power, as shown in Figs. 7(a) and 7(b). Moreover, with

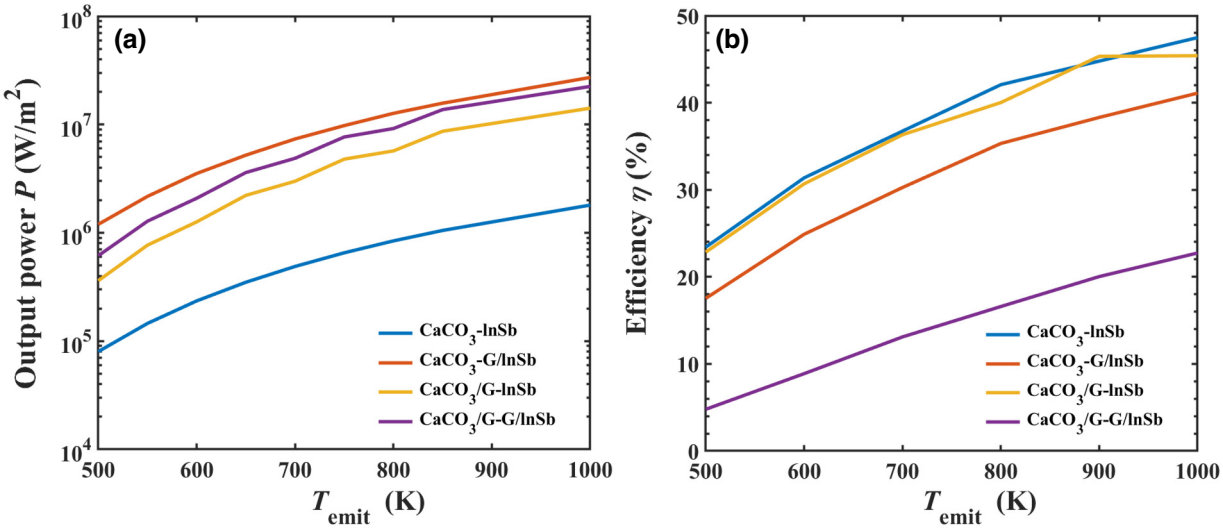

FIG. 9. The output power P and efficiency η vary with the temperature of the emitter T_{emit} for the four structures. (a) Output power. (b) Efficiency. Here, d is 20 nm.

the increase of thickness h, the normalized output power of $CaCO_3$-InSb and $CaCO_3$-G/InSb structures gradually increases. We note that the normalized output power of $CaCO_3$-InSb and $CaCO_3$-G/InSb structures can reach 84.3% and 96.2% at $h = 10\,000$ nm, respectively. Nevertheless, the efficiency of $CaCO_3$-InSb and $CaCO_3$-G/InSb structures gradually decreases, as shown in Figs. 8(a) and 8(b). Specifically, the output power of $CaCO_3$-InSb structures with $h = 100$ nm is only 0.20 W/cm^2 lower than that of semi-infinite structures, while the efficiency is increased by 12.2% (from 35.1% to 47.3%). A similar trend also appears in the $CaCO_3$-G/InSb structure. Compared with the output power of the semi-infinite thickness, the output power of the thermal emitter with $h = 100$ nm decreases only by 0.39 W/cm^2, while the efficiency is increased by 1.4% (from 36.9% to 38.3%). Thus, to consider the output power and efficiency, we set the thickness of the thermal emitter of the two structures to 100 nm.

In addition, compared with other thicknesses, the $CaCO_3$/G-InSb and $CaCO_3$/G-G/InSb structures with thermal emitter thicknesses of 10 nm have higher SHF above the band gap frequency, which contributes large output power, as shown in Figs. 7(c) and 7(d). We also note that the two structures with thermal emitter thicknesses of 10 nm have a lesser parasitic loss under the band gap frequency than other thicknesses. Therefore, we set the thickness of the thermal emitter of the two structures to 10 nm. The above results show that the thickness change of the thermal emitter has more significant effects on the performance of NFTPV devices.

To evaluate the performance of four structures at different temperatures, we calculated the output power and efficiency of structures when T_{emit} is between 500 and 1000 K, as shown in Fig. 9. Moreover, we set $h = 100$ nm in $CaCO_3$-InSb and $CaCO_3$-G/InSb structures, set $h = 10$ nm in $CaCO_3$/G-InSb and $CaCO_3$/G-G/InSb structures. The output power and efficiency of the four structures increase with the temperature of the thermal emitter. The output power of $CaCO_3$-G/InSb structures reaches 27.2 W/cm^2 due to the coupling effect of HPhPs in $CaCO_3$ and SPPs in graphene when $T_{\text{emit}} = 1000$ K, $d = 20$ nm. Nevertheless, the output power of $CaCO_3$-InSb structures is 1.8 W/cm^2, which is only 6.6% of that of $CaCO_3$-G/InSb structures, as shown in Fig. 9(a). In addition, as shown in Fig. 9(b), although $CaCO_3$-InSb and $CaCO_3$/G-InSb structures have high efficiency, the output power of the two structures is lower, while the $CaCO_3$-G/InSb structure has both high output power (27.2 W/cm^2) and high efficiency (41.1%) when $T_{\text{emit}} = 1000$ K, $d = 20$ nm. Due to the wide spectrum emission above the band gap and a large number of parasitic losses under the band gap, the $CaCO_3$/G-G/InSb structure has high output power, but also the efficiency is greatly limited.

IV. CONCLUSIONS

In conclusion, our proposed NFTPV device utilizing $CaCO_3$ as the thermal emitter and InSb p-n junction as the PV cells demonstrate promising performance. Through the comparison of four different structures, we find that the $CaCO_3$-G/InSb structure exhibits the best performance based on the assumption of considering only radiative recombination, achieving a high efficiency of 41% and an impressive output power density of 94 W/cm^2 when the thermal emitter temperature is set at 900 K. The improved performance can be attributed to the frequency coupling between the hyperbolic resonance and the interband transition of InSb p-n junction, where the SPPs

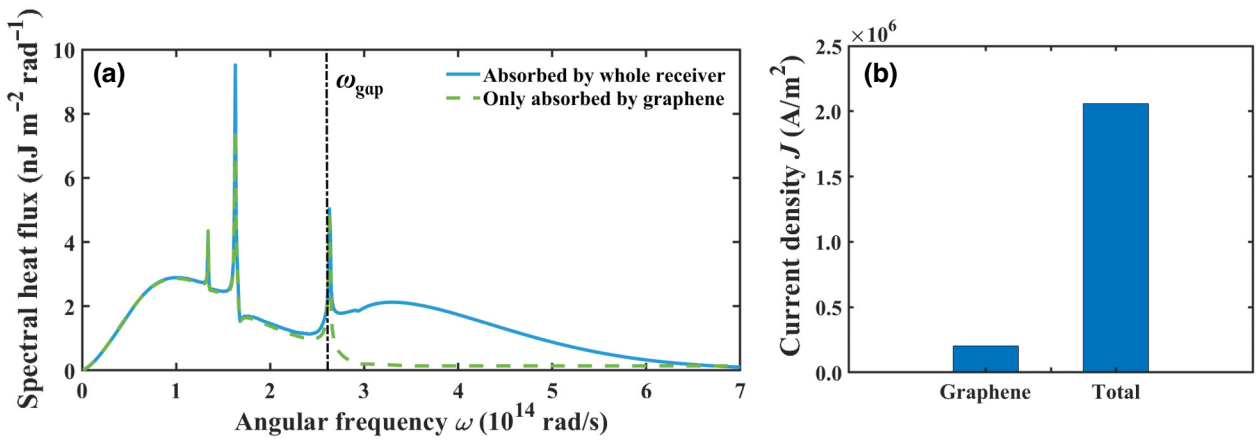

FIG. 10. (a) SHF absorbed by the whole receiver and that only absorbed by graphene vary with angular frequency. (b) Current density generated in graphene and whole receiver. The $\omega_{gap} = 2.62 \times 10^{14}$ rad/s, the T_{emit} is 900 K, T_{cell} is 300 K, and the thermal emitter is bulk. The OA of $CaCO_3$ is along the z axis, $V = 0$.

excited in graphene make a promotion role. Our work also investigates the impacts of the gap distance, thermal emitter temperature, and emitter thickness on the performance of the NFTPV device. The research could be beneficial for understanding the coupling of SPPs and HPhPs and designing high-performance thermophotovoltaic devices.

ACKNOWLEDGMENTS

This work is supported by the National Natural Science Foundation of China (52106099), the Natural Science Foundation of Shandong Province (ZR2022YQ57), National Natural Science Foundation of China (No. 12004327), and the Taishan Scholars Program.

APPENDIX A: CALCULATION OF THE REDIATIVE HEAT FLUX ABSORBED BY THE GRAPHENE LAYER

Radiative heat flux may also be absorbed by the graphene layer covering the surface of the InSb PV cell due to the highly confined surface mode. We analyze the radiative heat flux absorbed by the graphene layer by analyzing the SHF of the $CaCO_3$/G-G/InSb structure, as shown in Fig. 10(a). It clearly can be found that the SHF under the band gap is mainly absorbed by the graphene layer, while the SHF above the band gap is less absorbed by the graphene layer. We also calculate that the useful photon absorbed by the graphene layer is only 10% of that absorbed by the receiver composed of graphene and InSb PV cell, as shown in Fig. 10(b). Although the output power

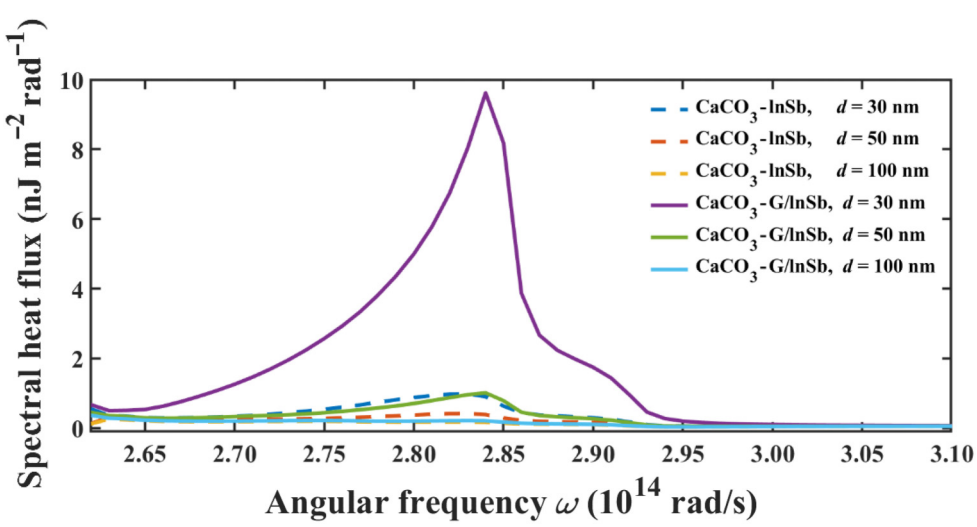

FIG. 11. SHFs of $CaCO_3$-InSb and $CaCO_3$-G/InSb structures above the band gap vary with angular frequency for different gap distances d. Here, T_{emit} is 900 K, T_{cell} is 300 K, and the thermal emitter is bulk.

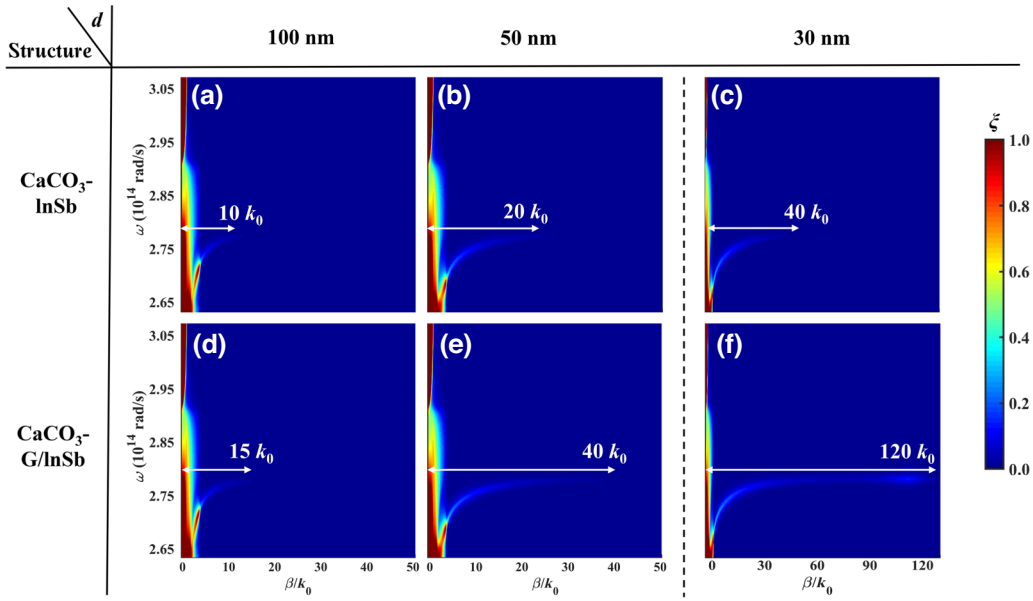

FIG. 12. ETCs of $CaCO_3$-InSb and $CaCO_3$-G/InSb structures for different gap distances d vary with angular frequency and dimensionless wavevector. The T_{emit} is 900 K, T_{cell} is 300 K, and the thermal emitter is bulk.

of the $CaCO_3$/G-G/InSb structure is significantly boosted, the efficiency is low due to the parasitic loss resulting from the coupling of SPPs under the band gap. Moreover, $CaCO_3$-G/InSb and $CaCO_3$/G-G/InSb have higher output power due to the graphene layer covering the InSb PV cell. The efficiency of the $CaCO_3$-G/InSb structure is higher than the $CaCO_3$/G-G/InSb structure, which is due to the absence of a graphene layer on $CaCO_3$, resulting in the lack of parasitic loss resulting from the coupling of SPPs under the band gap. The ETCs in Figs. 6(b) and 6(d) can also explain these phenomena.

APPENDIX B: PERFORMANCES OF THE $CaCO_3$-InSb AND $CaCO_3$-G/InSb STRUCTRUES VARY WITH GAP DISTANCE

To further investigate the gap distance on the performances of $CaCO_3$-InSb and $CaCO_3$-G/InSb, we calculate the SHFs of $CaCO_3$-InSb and $CaCO_3$-G/InSb structures for different gap distances. Figure 11 shows the SHFs of $CaCO_3$-InSb and $CaCO_3$-G/InSb structures for different gap distances. When the gap distance is 100 nm, the SHFs of $CaCO_3$-InSb and $CaCO_3$-G/InSb structures above the frequency of the band gap are almost unchanged. With

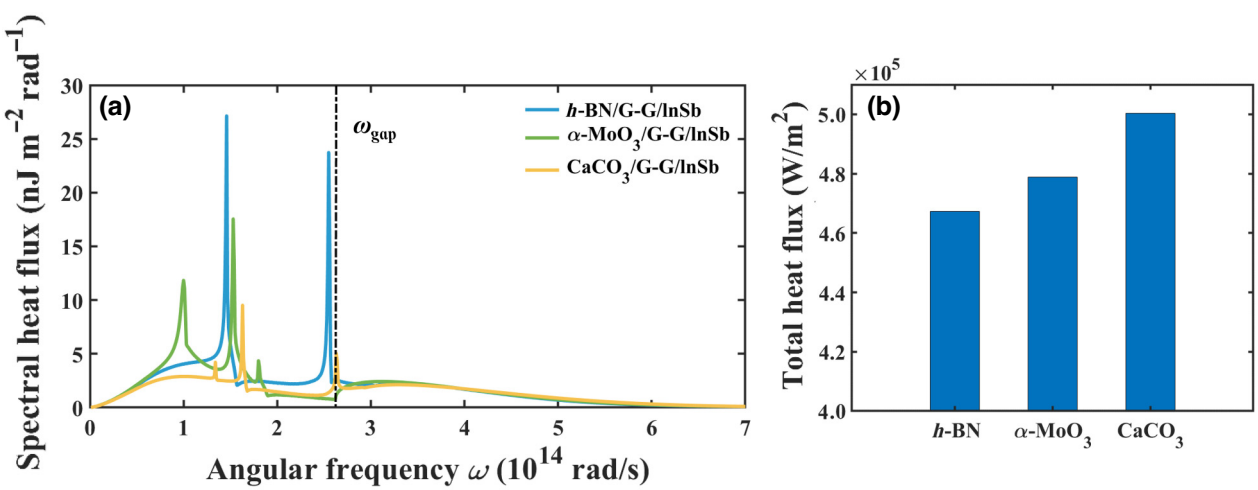

FIG. 13. (a) SHFs of h-BN/G-G/InSb, α-MoO_3/G-G/InSb, and $CaCO_3$/G-G/InSb structures vary with angular frequency. (b) The total heat flux above the band gap for different structures. Here, T_{emit} is 900 K, T_{cell} is 300 K, and the thermal emitter is bulk.

the decrease in gap distance ($d = 30$ nm), the SHF of the $CaCO_3$-G/InSb structure is obviously improved. To elucidate the underlying physical mechanisms of the difference in the performance of NFTPV devices, we further calculate the ETCs as a function of angular frequency and dimensionless wave vector for different structures. As shown in Figs. 12(c) and 12(f), the ETC of the $CaCO_3$-G/InSb structure extends to higher wavevector space (approximately equal to 120 k_0) at small gap distance due to the coupling of HPhPs in the $CaCO_3$ and SPPs in the graphene layer. However, the ETC of the $CaCO_3$-InSb structure changes inconspicuously for different gap distances, as shown in Figs. 12(a) and 12(b). Thus, the performance of $CaCO_3$-G/InSb structure improved significantly with the decreasing gap distance.

APPENDIX C: PERFORMANCE ANALYSIS OF DIFFERENT HYPERBOLIC MATERIALS USED AS THERMAL EMITTERS IN NFTPV SYSTEMS

To further investigate the performances of *h*-BN/G-G/InSb, α-MoO_3/G-G/InSb, and $CaCO_3$/G-G/InSb structures, we calculate the SHFs for different structures. Figure 13(a) shows the SHFs of *h*-BN/G-G/InSb, α-MoO_3/G-G/InSb, and $CaCO_3$/G-G/InSb structures. It can be easily found that the parasitic loss under the frequency of band gap for *h*-BN/G-G/InSb and α-MoO_3/G-G/InSb structures are more excessive than that for $CaCO_3$/G-G/InSb structure. The large parasitic loss results in low conversion efficiency. Moreover, more heat flux between $CaCO_3$/G-G/InSb structure is located in the frequency range above the frequency of the band gap, having the potential to generate more output power, as shown in Fig. 13(b). Thus, the $CaCO_3$ is more suitable than *h*-BN and α-MoO_3 for the proposed NFTPV system in this work as a thermal emitter.

[1] K. Chen, P. Santhanam, and S. Fan, Suppressing sub-bandgap phonon-polariton heat transfer in near-field thermophotovoltaic devices for waste heat recovery, Appl. Phys. Lett. **107**, 091106 (2015).

[2] F. Chen, X. Liu, Y. Tian, J. Goldsby, and Y. Zheng, Refractory all-ceramic thermal emitter for high-temperature near-field thermophotovoltaics, Energies **15**, 1830 (2022).

[3] C. Ferrari, F. Melino, M. Pinelli, P. Spina, and M. Venturini, Overview and status of thermophotovoltaic systems, Energy Procedia **45**, 160 (2014).

[4] A. LaPotin, K. Schulte, M. Steiner, K. Buznitsky, C. Kelsall, and D. Friedman, Thermophotovoltaic efficiency of 40%, Nature **604**, 287 (2022).

[5] C. Lucchesi, D. Cakiroglu, J. Perez, T. Taliercio, E. Tournie, and P. Chapuis, Near-field thermophotovoltaic conversion with high electrical power density and cell efficiency above 14, Nano Lett. **21**, 4524 (2021).

[6] Y. Matsuno, N. Nagumo, M. Araki, K. Yada, K. Yamaga, and A. Sakurai, Non-equilibrium mid-infrared black phosphorus light emitter and absorber for thermophotonic applications, J. Quant. Spectrosc. Radiat. Transfer **288**, 108271 (2022).

[7] W. Hsu, J. Tong, B. Liao, Y. Huang, S. Boriskina, and G. Chen, Entropic and near-field improvements of thermoradiative cells, Sci. Rep. **6**, 34837 (2016).

[8] R. Messina and P. Ben-Abdallah, Graphene-based photovoltaic cells for near-field thermal energy conversion, Sci. Rep. **3**, 1383 (2013).

[9] J. Song, J. Han, M. Choi, and B. Lee, Modeling and experiments of near-field thermophotovoltaic conversion: A review, Sol. Energy Mater. Sol. Cells **238**, 111556 (2022).

[10] Z. Yang, H. Li, Y. Wang, X. Chen, and J. Chen, Performance comparison of near- and far-field temperature-dependent thermophotovoltaic systems with tungsten emitter and $Ga_xIn_{1-x}As$ cell, Energy Convers. Manag. **257**, 115416 (2022).

[11] A. Datas, A. Ramos, A. Martí, C. del Cañizo, and A. Luque, Ultra high temperature latent heat energy storage and thermophotovoltaic energy conversion, Energy **107**, 542 (2016).

[12] C. Amy, H. Seyf, M. Steiner, D. Friedman, and A. Henry, Thermal energy grid storage using multi-junction photovoltaics, Energy Environ. Sci. **12**, 334 (2019).

[13] R. Bhatt, I. Kravchenko, and M. Gupta, High-efficiency solar thermophotovoltaic system using a nanostructure-based selective emitter, Sol. Energy **197**, 538 (2020).

[14] Z. Zhou, E. Sakr, Y. Sun, and P. Bermel, Solar thermophotovoltaics: Reshaping the solar spectrum, Nanophotonics **5**, 1 (2016).

[15] N. Harder and P. Würfel, Theoretical limits of thermophotovoltaic solar energy conversion, Semicond. Sci. Technol. **18**, S151 (2003).

[16] J. Song, M. Choi, Z. Yang, J. Lee, and B. Lee, A multi-junction-based near-field solar thermophotovoltaic system with a graphite intermediate structure, Appl. Phys. Lett. **121**, 163503 (2022).

[17] K. Mustafa, S. Abdullah, M. Abdullah, and K. Sopian, A review of combustion-driven thermoelectric (TE) and thermophotovoltaic (TPV) power systems, Renewable Sustainable Energy Rev. **71**, 572 (2017).

[18] W. Chan, V. Stelmakh, M. Ghebrebrhan, M. Soljačić, J. Joannopoulos, and I. Čelanović, Enabling efficient heat-to-electricity generation at the mesoscale, Energy Environ. Sci. **10**, 1367 (2017).

[19] D. Vance, S. Nimbalkar, A. Thekdi, K. Armstrong, T. Wenning, and J. Cresko, Estimation of and barriers to waste heat recovery from harsh environments in industrial processes, J. Cleaner Prod. **222**, 539 (2019).

[20] Z. Zhang, C. Fu, and X. Wu, Influence of hBN orientation on the near-field radiative heat transfer between graphene/hBN heterostructures, J. Photonics Energy **9**, 032702 (2018).

[21] K. Shi, F. Bao, and S. He, Enhanced near-field thermal radiation based on multilayer graphene-hBN heterostructures, ACS Photonics **4**, 971 (2017).

[22] L. Tang, J. DeSutter, and M. Francoeur, Near-field radiative heat transfer between dissimilar materials mediated

by coupled surface phonon- and plasmon-polaritons, ACS Photonics **7**, 1304 (2020).

[23] K. Shi, Y. Sun, Z. Chen, N. He, F. Bao, J. Evans, and S. He, Colossal enhancement of near-field thermal radiation across hundreds of nanometers between millimeter-scale plates through surface plasmon and phonon polaritons coupling, Nano Lett. **19**, 8082 (2019).

[24] H. Hajian, I. Rukhlenko, V. Erçağlar, G. Hanson, and E. Ozbay, Epsilon-near-zero enhancement of near-field radiative heat transfer in BP/hBN and BP/α-MoO3 parallel-plate structures, Appl. Phys. Lett. **120**, 112204 (2022).

[25] X. Wu and C. Fu, Near-field radiative heat transfer between uniaxial hyperbolic media: Role of volume and surface phonon polaritons, J. Quant. Spectrosc. Radiat. Transfer **258**, 107337 (2021).

[26] X. Wu and C. Fu, Hyperbolic volume and surface phonon polaritons excited in an ultrathin hyperbolic slab: connection of dispersion and topology, Nanoscale Microscale Thermophys. Eng. **25**, 64 (2021).

[27] X. Wu, C. Fu, and Z. Zhang, Near-field radiative heat transfer between two α-MoO_3 biaxial crystals, J. Heat Transfer **142**, 072802 (2020).

[28] S. Dai, Z. Fei, Q. Ma, S. Rodin, M. Wagner, S. McLeod, K. Liu, W. Gannett, W. Regan, K. Watanabe, T. Taniguchi, M. Thiemens, G. Dominguez, C. Neto, A. Zettl, F. Keilmann, J. Herrero, M. Fogler, and N. Basov, Tunable phonon polaritons in atomically thin van der Waals crystals of boron nitride, Science **343**, 1125 (2014).

[29] D. Caldwell, V. Kretinin, Y. Chen, V. Giannini, M. Fogler, Y. Francescato, T. Ellis, G. Tischler, R. Woods, J. Giles, M. Hong, K. Watanabe, T. Taniguchi, A. Maier, and S. Novoselov, Hyperbolic phonon-polaritons in boron nitride for near-field optical imaging and focusing, Nat. Commun. **5**, 5221 (2014).

[30] T. Low, A. Chaves, D. Caldwell, A. Kumar, X. Fang, P. Avouris, F. Heinz, F. Guinea, M. Moreno, and F. Koppens, Polaritons in layered two-dimensional materials, Nat. Mater. **16**, 182 (2017).

[31] K. Korzeb, M. Gajc, and A. Pawlak, Compendium of natural hyperbolic materials, Opt. Express **23**, 25406 (2015).

[32] J. Sun, M. Litchinitser, and J. Zhou, Indefinite by nature: From ultraviolet to terahertz, ACS Photonics **1**, 293 (2014).

[33] G. Baranov, H. Edgar, T. Hoffman, N. Bassim, and D. Caldwell, Perfect interferenceless absorption at infrared frequencies by a van der Waals crystal, Phys. Rev. B **92**, 201405 (2015).

[34] G. Folland, W. Maß, R. Matson, R. Nolen, S. Liu, K. Watanabe, T. Taniguchi, H. Edgar, T. Taubner, and D. Caldwell, Probing hyperbolic polaritons using infrared attenuated total reflectance micro-spectroscopy, MRS Commun. **8**, 1418 (2018).

[35] R. Wang, J. Lu, and J. Jiang, Enhancing thermophotovoltaic performance using graphene-BN-InSb near-field heterostructures, Phys. Rev. Appl. **12**, 044038 (2019).

[36] A. Karalis and J. Joannopoulos, Temporal coupled-mode theory model for resonant near-field thermophotovoltaics, Appl. Phys. Lett. **107**, 141108 (2015).

[37] J. Zhang, Y. Hu, Q. Han, H. Liu, Y. Sun, and X. Wu, Optical axis-driven modulation of near-field radiative heat transfer between two calcite parallel structures, Phys. Chem. Chem. Phys. **24**, 22102 (2022).

[38] B. Zhao, Z. Zhang, and S. Fan, Near-field heat transfer between graphene/hBN multilayers, Phys. Rev. B **95**, 245437 (2017).

[39] B. Zhao and Z. Zhang, Enhanced photon tunneling by surface plasmon–phonon polaritons in graphene/hBN heterostructures, J. Heat Transfer **139**, 022701 (2017).

[40] A. Woessner, M. B. Lundeberg, Y. Gao, A. Principi, P. Alonso-González, M. Carrega, K. Watanabe, T. Taniguchi, G. Vignale, M. Polini, J. Hone, R. Hillenbrand, and F. Koppens, Highly confined low-loss plasmons in graphene–boron nitride heterostructures, Nat. Mater. **14**, 421 (2015).

[41] M. Shur, *Handbook Series on Semiconductor Parameters* (World Scientific, Singapore, 1996).

[42] D. Feng, E. Tervo, S. Yee, and Z. Zhang, Effect of evanescent waves on the dark current of thermophotovoltaic cells, Nanoscale Microscale Thermophys. Eng. **24**, 1 (2020).

[43] J. Pendry, Negative refraction makes a perfect lens, Phys. Rev. Lett. **85**, 3966 (2000).

[44] Y. Zhang, C. Wang, H. Yi, and H. Tan, Multiple surface plasmon polaritons mediated near-field radiative heat transfer between graphene/vacuum multilayers, J. Quant. Spectrosc. Radiat. Transfer **221**, 138 (2018).

[45] M. Lim, S. Jin, S. Lee, and B. Lee, Graphene-assisted Si-InSb thermophotovoltaic system for low temperature applications, Opt. Express **23**, A240 (2015).

[46] B. Zhao, K. Chen, S. Buddhiraju, G. Bhatt, M. Lipson, and S. Fan, High-performance near-field thermophotovoltaics for waste heat recovery, Nano Energy **41**, 344 (2017).

[47] N. Ashcroft and N. Mermin, *Solid State Physics* (Cengage Learning, Philadelphia, 1976).

[48] H. Hajian, I. Rukhlenko, G. Hanson, T. Low, B. Butun, and E. Ozbay, Tunable plasmon-phonon polaritons in anisotropic 2D materials on hexagonal boron nitride, Nanophotonics **9**, 3909 (2020).

[49] H. Hajian, I. Rukhlenko, G. Hanson, and E. Ozbay, Hybrid surface plasmon polaritons in graphene coupled anisotropic van der Waals material waveguides, J. Phys. D: Appl. Phys. **54**, 455102 (2021).

[50] M. Laroche, R. Carminati, and J. Greffet, Near-field thermophotovoltaic energy conversion, J. Appl. Phys. **100**, 063704 (2006).

[51] S. Chen, H. Liu, B. Wu, X. Wu, and C. Fu, Comparative analysis of two models for the optical response of a thin slab: a film of finite thickness versus a surface current sheet, Phys. Chem. Chem. Phys. **25**, 6194 (2023).

[52] Y. Hu, B. Wu, H. Liu, B. Yang, D. Zhang, Y. Sun, and X. Wu, Near-field radiative modulator driven by anisotropic hyperbolic polaritons in biaxial hyperbolic materials, J. Quant. Spectrosc. Radiat. Transfer **296**, 108468 (2023).

[53] K. Yu, L. Li, K. Shi, H. Liu, Y. Hu, K. Zhang, Y. Liu, and X. Wu, Near-field radiative heat transfer between multilayer structures composed of different hyperbolic materials, Int. J. Heat Mass Transfer **211**, 124229 (2023).

[54] L. Li, X. Wu, H. Liu, K. Shi, Y. Liu, and K. Yu, Near-field radiative modulator based on α-MoO_3 films, Int. J. Heat Mass Transfer **216**, 124603 (2023).